*Progress In Electromagnetics Research B, Vol. 67, 107–120, 2016*

# Application of Facet Scattering Model in SAR Imaging of Sea Surface Waves with Kelvin Wake

**Jia-Kun Wang*, Min Zhang, Jun-Long Chen, and Zhao-Hui Cai**

**Abstract**—The principal purpose of this work is the simulation of the ship wake in Synthetic Aperture Radar (SAR) imaging based on a facet scattering model. The hydrodynamic model of the surface waves mainly considers the Kelvin wake waves and the wind driven waves. For the prediction of radar returns from the composite surface, the semi-deterministic facet scattering model (SDFSM) is proposed, which is verified to have good performance through a comparison with the experiment by SASS-II. Then, the distributions of backscattering normalized radar cross section (NRCS) of facets are investigated for both $VV$ and $HH$ polarizations and characteristics of the wake pattern are shown with good visibility. On the basis of these, an application of velocity bunching (VB) imaging model is presented in detail for the simulation of SAR imaging of sea surface waves with Kelvin wake. Finally, several numerical results provide states of the effects of ship speed, wind speed and the ship sailing direction on the characteristics of Kelvin wake in SAR images. Thus, this simulation may enable us to provide a theoretical basis to the detection of ship wakes.

## 1. INTRODUCTION

Synthetic Aperture Radar (SAR) imaging has been proved to be a significant technique for the study of sea surface waves. A summarization including the mechanism of radar scattering and SAR imaging of the sea surface was concluded by Holt [1]. One of the most important applications of radar imaging of sea surface is ship detection and location by means of signal processing technology [2, 3]. It has been generally accepted that the visibility of the sea surface wave in the SAR images is mainly due to their impact on the radar backscattered cross-section attributed to the tilt and hydrodynamic modulations. Besides, the velocity bunching effect also enables the surface waves to be visible on SAR images.

Ship wakes are often more visible than the ships themselves in SAR images of ocean surface obtained from space borne or airborne radars [4–6], which is of great significance to ship detection and classification. As a result of a careful examination of the experienced data and some theoretical analysis, it appears that the wake waves can mainly be classified into three categories, such as the ship-generated Kelvin wave wakes, turbulent wakes and the internal waves. Actually, not all these features can be observed simultaneously in SAR images, depending on the radar parameters, environmental conditions as well as the ship's movements. Considering the specific movements of the Kelvin waves, the wake usually consists of two different wave classes including the transverse and divergent waves. The entire Kelvin wave wake is confined by two cusp lines at an angle less than the critical Kelvin angle of 39°. However, turbulent wakes are most frequently observable feature in SAR images displayed as a dark and narrow line along the ship track. As for the occurrence of this phenomenon, it has not been well understood yet. Besides, the emergence of the internal waves is under certain conditions such as an existence of a stratification of water density in horizontal layers. And the internal waves, once generated, can propagate for a long distance. In this study, we focus mainly on the Kelvin wake.

*Received 28 February 2016, Accepted 21 April 2016, Scheduled 5 May 2016*
* Corresponding author: Jia-Kun Wang (wangjiakun1989@163.com).
The authors are with the School of Physics and Optoelectronic Engineering, Xidian University, Xi'an, China.

Since the formulation of fluid dynamic theory was firstly concluded mathematically by Lord Kelvin, there have been a lot of scholars to do researches focusing on the Kelvin wakes [7–15]. Based on the Bragg mechanism of sea surface, Tunaley et al. [7] researched the SAR imaging of ship wakes in L-band and analyzed its validity through a comparison with the SeaSAT SAR imagery. Oumansour et al. [8] investigated the SAR imaging of ship wakes in X- and L-band utilizing the small perturbation scattering model. Shemer et al. [9] described a mathematical model to imaging the ship wakes with the help of interferometric SAR (INSAR) technique. Henning et al. [10] gave an explanation for the principle of SAR imaging of Kelvin arms and discussed the simulated results with experiments. Recently, Arnold-Bos et al. [13] developed a bistatic, polarimetric radar simulator for estimating pseudo-raw radar echoes of ship wakes that can be further processed for bistatic SAR (BiSAR) imaging. The detectability of the boundaries of Kelvin wake in SAR images is studied with the application of discrete Radon transform by Zilman et al. [15].

Extensive literatures have been devoted to analyze the electromagnetic scattering from a rough surface [16, 17]. The small perturbation method (SPM) was firstly introduced for the scattering from rough surfaces, which is a perturbative expansion of the scattering amplitude with respect to a small height parameter [18, 19]. The main limitation of the SPM is its restricted domain of validity, as it is valid for small root-mean-square (RMS) height/wavelength ratios. However, the SPM constitutes the reference for any approximate method in the low-frequency limit. As a unified model, the two-scale model (TSM) was developed to deal with surfaces with descriptions of capillary waves and gravity waves [20]. In this model, the scattering is decomposed into two terms: the first term uses the geometrical optical (GO) for modeling the contribution of the large scales, and the second term uses the first order SPM (SPM1) for modeling the contribution of the short scales. This model is simple to implement, but it is necessary to appropriately choose the surface cut-off wavenumber $k_c$ separating the contributions from the short scales and the large scales. It is also lack of consideration of the local characteristics of a special sea surface. Actually, the local fluctuation is always thought as an important feature in ocean SAR imaging. The commonly used method, SSA [21, 22], is applicable for a surface RMS slope lower than the slopes and surfaces with gentle slopes. It can readily be applied to surfaces having several scales of roughness. However, this model is not easy to implement numerically for its low efficiency in the computation of integral. Therefore, an effective facet-model method which breaks the surface into arbitrary titled small facets with local configurations as well as a numerical elevation representation is presented for the scattering analysis and radar imaging of surface waves in this paper.

The remainder of this paper is structured as follows. In Section 2, formulation for hydrodynamic model of sea surface waves with ship generated Kelvin wake is briefly introduced. In Section 3, a semi-deterministic facet scattering model is proposed for the estimation of backscattering from the surface wave. In Section 4, the construction of SAR imaging mechanism for ship wakes is given by the velocity bunching model. In Section 5, numerical simulations of SAR images of surface waves are investigated for several related parameters. Analysis demonstrates that the visibility of the wake pattern in SAR image is closely related to ship's movement as well as sea clutter parameters. Section 6 concludes this article.

## 2. HYDRODYNAMIC MODEL OF SURFACE WAVES

For the fully developed infinite-depth sea, the spectral method is applied to yield the wind dependent sea waves through a linear superposition of harmonic waves. The sea surface elevation $h_s$ at position $\mathbf{r} = (x, y)$ and time $t$ can be expressed as [23]

$$h_s(\mathbf{r}, t) = \sum_{\mathbf{k}} H(\mathbf{k}, t) \exp(j\mathbf{k} \cdot \mathbf{r}) \tag{1}$$

where $\mathbf{k} = (k_m, k_n)$ is a 2-D vector with components of $k_m = m\delta k_x$ and $k_n = n\delta k_y$. $m$ and $n$ are integers with bounds $-M/2 \leq m < M/2$ and $-N/2 \leq n < N/2$. $M$ and $N$ are the sampling numbers discretized at equal interval along $x$-axis and $y$-axis directions. The sampling intervals $\delta k_y = 2\pi/L_y$ and $\delta k_x = 2\pi/L_x$ are related to the lengths of the 2-D sea surface $L_x$ and $L_y$. The Fourier amplitudes

$H(\mathbf{k},t)$ of a sea surface elevation can be expressed as

$$\begin{aligned} H(\mathbf{k},t) &= \Upsilon(\mathbf{k})\sqrt{\Phi(\mathbf{k},\varphi)\delta k_x \delta k_y/2}\exp\left(-j\omega(\mathbf{k})t\right) \\ &\quad +\Upsilon^*(-\mathbf{k})\sqrt{\Phi(\mathbf{k},\pi-\varphi)\delta k_x \delta k_y/2}\exp\left(j\omega(-\mathbf{k})t\right) \end{aligned} \tag{2}$$

where $\Phi(\mathbf{k},\varphi)$ is the 2-D sea spectrum related to the wind speed$U$and direction $\varphi$ and the Elfouhaily spectrum [24] is adopted in this paper. $\Upsilon(\mathbf{k})$ is a complex normal distributed random series and "*" represents the conjugation operation. The relationship between wave angular frequency and wave number is ensured by the dispersion relation $\omega^2 = gk(1+k^2/k_p^2)$.

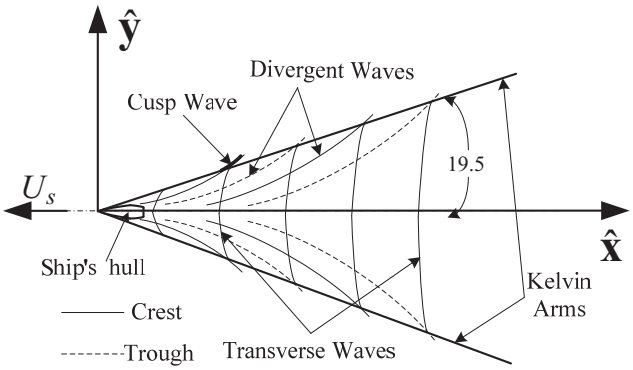


**Figure 1.** Kelvin wake pattern of transverse and divergent waves.

The wave patterns of Kelvin wake mainly comprise the transverse and divergent waves, as shown in Figure 1. Near the outer boundary, the interference between them forms the cusp wave. Assuming that the water is inviscid and incompressible, the flow about a point source can be described with the Green's function. By a combination of the Michell thin ship theory with the boundary conditions, the wave elevation in the far wake of a ship moving with speed $U_s$ can be written as follows [8]

$$h_k(x,y) = \mathrm{Re}\int_{-\pi/2}^{\pi/2} A(\theta)\exp[ik_0\sec^2\theta(x\cos\theta + y\sin\theta)]d\theta \tag{3}$$

where $k_0 = g/U_s^2$, $g$ is the acceleration due to gravity, $k_0\sec^2\theta$ the wave number of the waves travelling at angle $\theta$ with respect to the positve $x$-direction, and $A(\theta)$ the free spectrum representing the ship's characteristic and can be written according to the Kochin function as

$$A(\theta) = \frac{k_0\sec^3\theta}{\pi U_s}\iint\limits_{S_H} q(x,z)\exp\left[k_0\sec^2\theta(z-ix\cos\theta)\right]dxdz \tag{4}$$

$q(x,z) = -2U_s\frac{\partial\eta(x,z)}{\partial x}$, and the integration is performed over the submerged portion of the ship's center plane $S_H$. Here a Wigley parabolic ship of length $L$, beam $B$, and draft $T$ is used in the simulation

$$\eta(x,z) = \pm B\left[1-(2x/L)^2\right]\Big/2 \quad \text{for} \quad |x| \le L/2 \quad \text{and} \quad -T \le z \le 0 \tag{5}$$

However, the free surface wave height $h(\mathbf{r})$ is presented as a sum of the wave pertaining to wind-driven at a certain time, say $t=0$, and to the moving ship.

$$h(\mathbf{r}) = h_s(\mathbf{r},0) + h_k(\mathbf{r}) \tag{6}$$

According to the theory above, Figure 2 shows several results of the theoretical model of the ship generated Kelvin wakes over both flat surface and wind-driven sea surface. The ship model used is measured 52.0 m in length and 5.9 m in beam with a draught of 3.5 m. Ship speeds are chosen as 5.0 m/s and 9.0 m/s while the wind speeds are set by 3.0 m/s and 5.0 m/s, respectively. The simulation

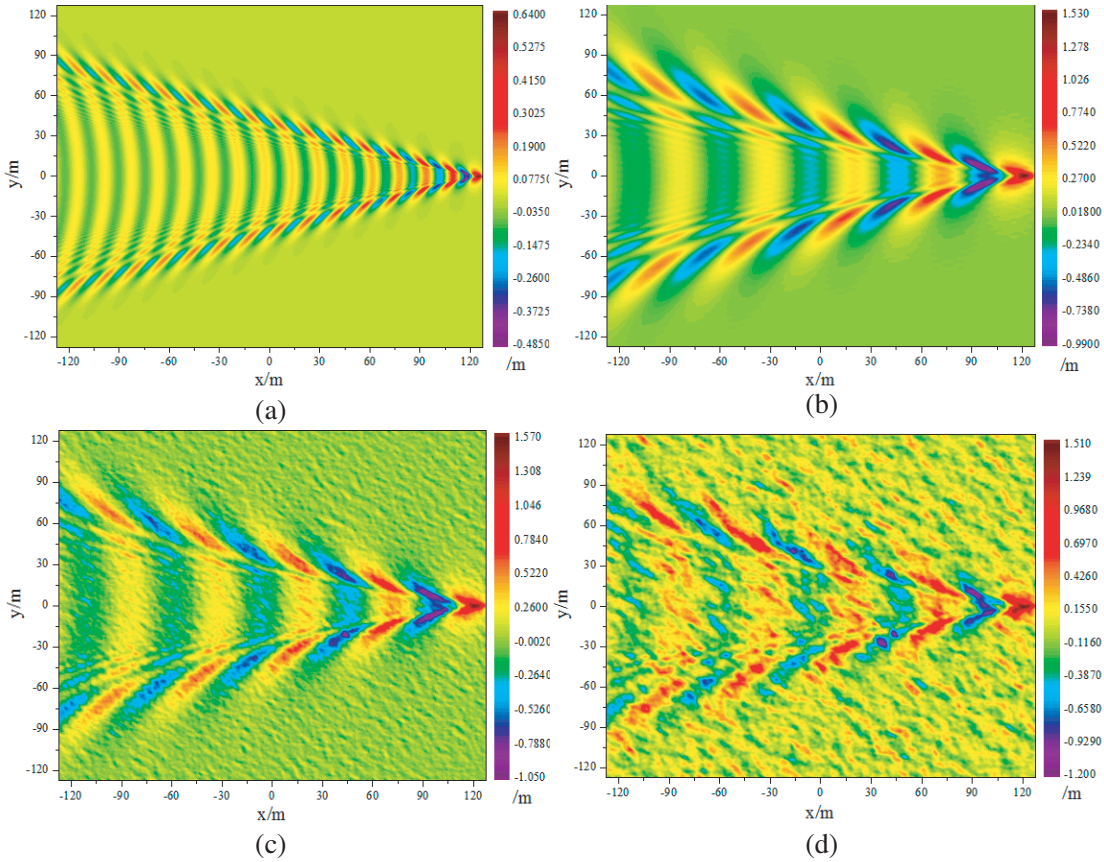


**Figure 2.** The simulated wave heights of Kelvin wake, (a), (b) over a flat surface with different ship speeds and (c), (d) over wind driven sea surface with different wind speeds. (a) Ship speed $U_s = 5.0\,\mathrm{m/s}$. (b) Ship speed $U_s = 9.0\,\mathrm{m/s}$. (c) Wind speed $U = 3.0\,\mathrm{m/s}$. (d) Wind speed $U = 5.0\,\mathrm{m/s}$.

area is $256\,\mathrm{m} \times 256\,\mathrm{m}$. It is evident that the ship generated Kelvin wake is mainly composed of transverse waves and divergent waves. As increase of the ship speed, both of the wavelengths tend to be greater as well as the wave height, as is shown in Figures 2(a) and (b). While the wake is over wind generated sea clutter, the wave distortion will appear in part of the wake wave due to its interaction with the wind waves, thus to influence its visibility especially under higher wind speed, see Figures 2(c) and (d), where the ship speed is $9.0\,\mathrm{m/s}$.

## 3. FACET MODEL FOR THE SCATTERING FIELD

Since the rough facets are statistically spatial homogeneous and the roughness of small scale wave on them is small enough, the scattering amplitude of a single facet illuminated by plane wave is given by the small perturbation method (SPM) [25–27]

$$\mathrm{S}_{pq}\left(\hat{\mathbf{k}}_i, \hat{\mathbf{k}}_s\right) = \frac{k^2(1-\varepsilon)}{8\pi^2}\mathrm{F}_{pq}\iint h(\mathbf{r})e^{-i\mathbf{q}\cdot\mathbf{r}}d\mathbf{r} \tag{7}$$

where, $\hat{\mathbf{k}}_i$ and $\hat{\mathbf{k}}_s$ are the unit vectors of incident and scattering waves, $\mathbf{q} = k(\hat{\mathbf{k}}_s - \hat{\mathbf{k}}_i)$, $k$ is the wavenumber of incident wave and $\varepsilon$ is the complex relative permittivity of sea water, the subscripts $p, q = h, v$ denote the polarization of incident and scattering waves. As a function of Fresnel reflection

coefficients, $R_v$ and $R_h$, the polarization factors $\mathrm{F}_{pq}$ can be expressed as

$$\begin{aligned}
\mathrm{F}_{vv} &= \frac{1}{\varepsilon}\left[1+R_v\left(\theta_i^l\right)\right]\left[1+R_v\left(\theta_s^l\right)\right]\sin\theta_i^l\sin\theta_s^l - \left[1-R_v\left(\theta_i^l\right)\right]\left[1-R_v\left(\theta_s^l\right)\right]\cos\theta_i^l\cos\theta_s^l\cos\phi_s^l \\
\mathrm{F}_{vh} &= \left[1-R_v\left(\theta_i^l\right)\right]\left[1+R_h\left(\theta_s^l\right)\right]\cos\theta_i^l\sin\phi_s^l \\
\mathrm{F}_{hv} &= \left[1+R_h\left(\theta_i^l\right)\right]\left[1-R_v\left(\theta_s^l\right)\right]\cos\theta_s^l\sin\phi_s^l \\
\mathrm{F}_{hh} &= \left[1+R_h\left(\theta_i^l\right)\right]\left[1+R_h\left(\theta_s^l\right)\right]\cos\phi_s^l
\end{aligned} \tag{8}$$

where $(\theta_i^l,\ \theta_s^l,\ \phi_s^l)$ are the local configuration angles defined in the local coordinate system $(\hat{\mathbf{x}}_l, \hat{\mathbf{y}}_l, \hat{\mathbf{z}}_l)$, as illustrated in Figure 3. Thus, by applying the definition of normalized radar cross section (NRCS), the NRCS of a single facet is given by

$$\sigma_{pq}^{SPM}\left(\hat{\mathbf{k}}_i, \hat{\mathbf{k}}_s\right) = \pi k^4 \left|\varepsilon - 1\right|^2 \left|\tilde{\mathrm{F}}_{pq}\right|^2 \Phi_E^{capi}\left(\mathbf{q}_l, \varphi\right) \tag{9}$$

where, $\Phi_E^{capi}(\mathbf{q}_l, \varphi)$ is the capillary wave part of Elfouhaily spectrum and $\mathbf{q}_l$ the projection vector of $\mathbf{q}$ on the local $\hat{\mathbf{x}}_l$, $\hat{\mathbf{y}}_l$ plane The global polarization factor $\tilde{\mathrm{F}}_{pq}$ based on $\mathrm{F}_{pq}$ can be expressed as

$$\begin{bmatrix} \tilde{\mathrm{F}}_{vv} & \tilde{\mathrm{F}}_{vh} \\ \tilde{\mathrm{F}}_{hv} & \tilde{\mathrm{F}}_{hh} \end{bmatrix} = \begin{bmatrix} \hat{\mathbf{V}}_s\cdot\hat{\mathbf{v}}_s & \hat{\mathbf{H}}_s\cdot\hat{\mathbf{v}}_s \\ \hat{\mathbf{V}}_s\cdot\hat{\mathbf{h}}_s & \hat{\mathbf{H}}_s\cdot\hat{\mathbf{h}}_s \end{bmatrix} \begin{bmatrix} \mathrm{F}_{vv} & \mathrm{F}_{vh} \\ \mathrm{F}_{hv} & \mathrm{F}_{hh} \end{bmatrix} \begin{bmatrix} \hat{\mathbf{V}}_i\cdot\hat{\mathbf{v}}_i & \hat{\mathbf{H}}_i\cdot\hat{\mathbf{v}}_i \\ \hat{\mathbf{V}}_i\cdot\hat{\mathbf{h}}_i & \hat{\mathbf{H}}_i\cdot\hat{\mathbf{h}}_i \end{bmatrix} \tag{10}$$

$\{\hat{\mathbf{H}}_i, \hat{\mathbf{V}}_i, \hat{\mathbf{H}}_s, \hat{\mathbf{V}}_s\}$ and $\{\hat{\mathbf{h}}_i, \hat{\mathbf{v}}_i, \hat{\mathbf{h}}_s, \hat{\mathbf{v}}_s\}$ are the unit polarization vectors under the global and local frame.

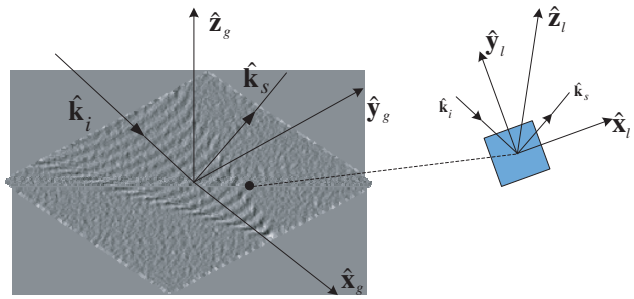


**Figure 3.** The geometry of the global and local frame for a facet on sea surface.

Considering the drawback of SPM in the region near vertical incidence, a supplement of Kirchhoff approximation (KA) [28] is used to make a correction. Thus, the NRCS of the facet can be rewritten as

$$\sigma_{pq}^{facet}\left(\hat{\mathbf{k}}_i, \hat{\mathbf{k}}_s\right) = \sigma_{pq}^{KA}\left(\hat{\mathbf{k}}_i, \hat{\mathbf{k}}_s\right) + \sigma_{pq}^{SPM}\left(\hat{\mathbf{k}}_i, \hat{\mathbf{k}}_s\right) \tag{11}$$

where

$$\sigma_{pq}^{KA}\left(\hat{\mathbf{k}}_i, \hat{\mathbf{k}}_s\right) = \frac{\pi k^2 \left|\mathbf{q}\right|^2}{q_z^4}\left|\tilde{\mathrm{F}}_{pq}^{KA}\right|^2 P\left(z_x, z_y\right) \tag{12}$$

The function $P(z_x, z_y)$ above is the probability density distribution (PDF) function and the corresponding slopes are denoted by $z_x = \partial h/\partial x$ and $z_y = \partial h/\partial y$. The polarization factors $\tilde{\mathrm{F}}_{pq}^{KA}$ of KA can be expressed as follows

$$\begin{aligned}
\tilde{\mathrm{F}}_{vv}^{KA} &= M_0\left[R_v\left(\theta_i^l\right)\left(\hat{\mathbf{V}}_s\cdot\hat{\mathbf{k}}_i\right)\left(\hat{\mathbf{V}}_i\cdot\hat{\mathbf{k}}_s\right) + R_h\left(\theta_i^l\right)\left(\hat{\mathbf{H}}_s\cdot\hat{\mathbf{k}}_i\right)\left(\hat{\mathbf{H}}_i\cdot\hat{\mathbf{k}}_s\right)\right] \\
\tilde{\mathrm{F}}_{vh}^{KA} &= M_0\left[R_v\left(\theta_i^l\right)\left(\hat{\mathbf{V}}_s\cdot\hat{\mathbf{k}}_i\right)\left(\hat{\mathbf{H}}_i\cdot\hat{\mathbf{k}}_s\right) - R_h\left(\theta_i^l\right)\left(\hat{\mathbf{H}}_s\cdot\hat{\mathbf{k}}_i\right)\left(\hat{\mathbf{V}}_i\cdot\hat{\mathbf{k}}_s\right)\right] \\
\tilde{\mathrm{F}}_{hv}^{KA} &= M_0\left[R_v\left(\theta_i^l\right)\left(\hat{\mathbf{H}}_s\cdot\hat{\mathbf{k}}_i\right)\left(\hat{\mathbf{V}}_i\cdot\hat{\mathbf{k}}_s\right) - R_h\left(\theta_i^l\right)\left(\hat{\mathbf{V}}_s\cdot\hat{\mathbf{k}}_i\right)\left(\hat{\mathbf{H}}_i\cdot\hat{\mathbf{k}}_s\right)\right] \\
\tilde{\mathrm{F}}_{vv}^{KA} &= M_0\left[R_v\left(\theta_i^l\right)\left(\hat{\mathbf{H}}_s\cdot\hat{\mathbf{k}}_i\right)\left(\hat{\mathbf{H}}_i\cdot\hat{\mathbf{k}}_s\right) + R_h\left(\theta_i^l\right)\left(\hat{\mathbf{V}}_s\cdot\hat{\mathbf{k}}_i\right)\left(\hat{\mathbf{V}}_i\cdot\hat{\mathbf{k}}_s\right)\right]
\end{aligned} \tag{13}$$

where, $M_0 = |\mathbf{q}||q_z|/\{[(\hat{\mathbf{H}}_s \cdot \hat{\mathbf{k}}_i)^2 + (\hat{\mathbf{V}}_s \cdot \hat{\mathbf{k}}_i)^2]kq_z\}$.

The total NRCS of a free surface can be given by

$$\sigma_{pq}\left(\hat{\mathbf{k}}_i, \hat{\mathbf{k}}_s\right) = \frac{1}{A}\sum_{m=1}^{M}\sum_{n=1}^{N}\left\{\sigma_{pq,mn}^{facet}\left(\hat{\mathbf{k}}_i, \hat{\mathbf{k}}_s\right)\Delta x \Delta y\right\} \tag{14}$$

$m$ and $n$ means the location of the facet center along the $x$-axis and $y$-axis by $x = m\Delta x$ and $y = n\Delta y$, respectively. Thus, the model discussed above is described as Semi-deterministic facet scattering model (SDFSM).

To verify the validation of SDFSM, Figure 4 illustrates the backscattering NRCS of wind driven wave through a comparison with the experiment by SASS-II [19] for both $VV$ and $HH$ polarizations for a frequency of 14.6 GHz at wind speeds 5.0 m/s and 10.0 m/s, respectively. It can be obviously seen that there is a good agreement between the model and the experiment in most instances. In addition, the distributions of backscattering NRCS at 14.6 GHz for every single facet are shown in Figure 5 which corresponds to the ship wake scenario in Figure 2(c). The incident angle is 40° and the flight direction is along the positive $y$-axis, which is consistent with Figure 6 and the following simulations. The results feature the texture of the wake pattern clearly and the NRCS of a facet for $VV$ polarization is always larger than for $HH$ polarization. The difference for the NRCS between $VV$ polarization and $HH$ polarization is mainly due to the effect of the polarization factor, which is strongly dependent on the local parameters of a facet. From the analysis of NRCS for both polarizations, the variation of $HH$ polarization NRCS with the slope of facet seems to be more sensitive than $VV$ polarization and the difference of NRCS between crest and trough is more notable for $HH$ polarization than $VV$ polarization. These explain that $HH$ polarization could reflect the texture feature more clearly.

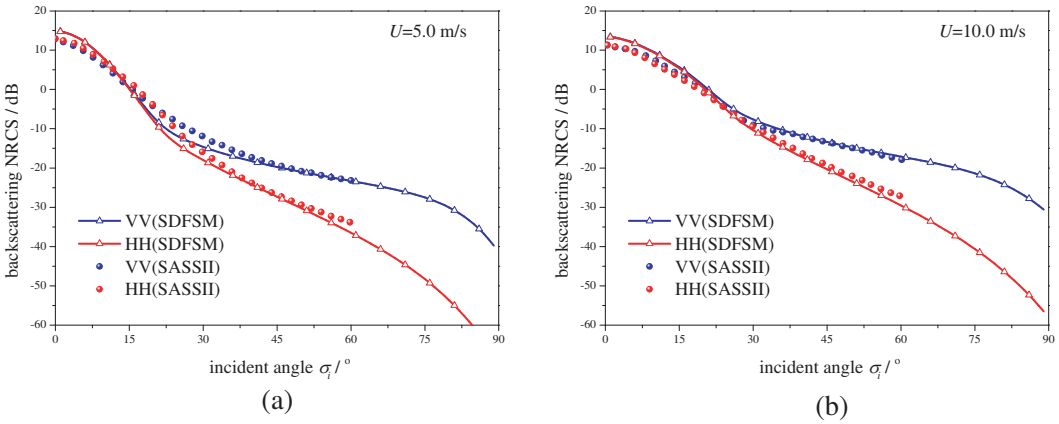


**Figure 4.** Backscattering NRCS comparison between SDFSM and the experiment SASS-II at 14.6 GHz for different wind speeds. (a) Wind speed 5.0 m/s. (b) Wind speed 10.0 m/s.

## 4. SAR IMAGE SIMULATION OF KELVIN WAVE WAKE

To proceed with SAR imaging of the scene containing wind wave and ship wake, the generalized velocity bunching model is invoked in this investigation for the image intensity averaged over the free surface waves. The geometric sketch is illustrated in Figure 6. As for the assumption of neglecting speckle, system noise and the range-azimuth coupling, the ensemble averaged SAR image intensity distribution $I(x, y)$ is given by [29–31]

$$\begin{aligned} I(x,y) \;=\; & \int_{-L_x/2}^{L_x/2}\int_{-L_y/2}^{L_y/2} dx_g dy_g \sigma_I(x_g, y_g) \\ & \cdot \frac{\rho_{aN}}{\rho'_{aN}(x_g, y_g)} \exp\left\{-\frac{\pi^2}{\rho'_{aN}(x_g, y_g)^2}\left[y - y_g - R \cdot u_r(x_g, y_g)/V\right]^2\right\}\delta(x - x_g) \end{aligned} \tag{15}$$

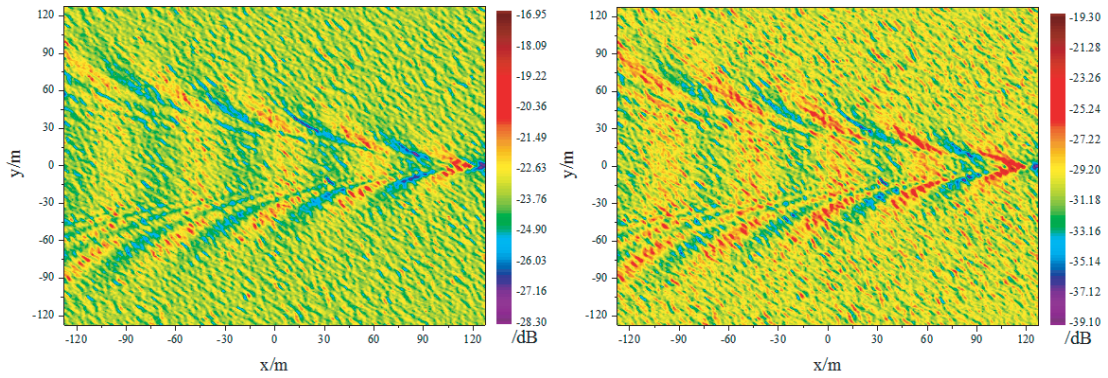


**Figure 5.** Distribution of facet backscattering coefficients at incident angle $\theta_i = 40°$. (a) $VV$ polarization. (b) $HH$ polarization

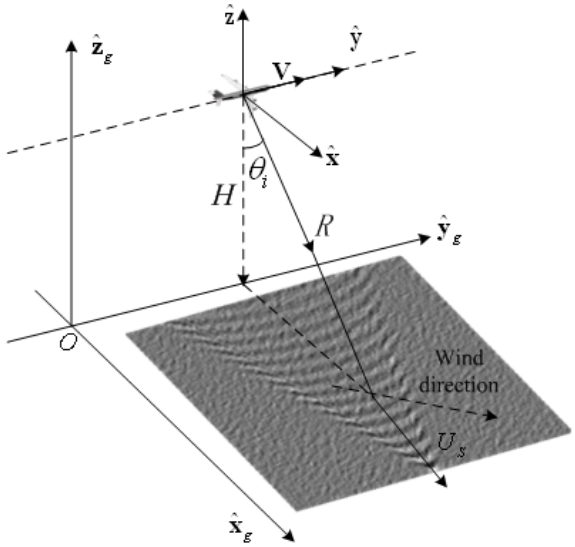


**Figure 6.** Model of SAR imagery of surface waves.

where, $u_r(x_g, y_g)$ means the radial component of the mean orbital velocity of a wave patch. $\sigma_I(x_g, y_g)$ is the mean NRCS of surface wave modified by tilt modulation and hydrodynamic modulation by the relationship $\sigma_I(x_g, y_g) = \sigma^{facet}(x_g, y_g)[1 + f_{\rm SAR}(x_g, y_g]$, $\sigma^{facet}$ is the scattering coefficient of a facet calculated by Eq. (11). $\rho_a = \lambda R/2VT_0$ is the full-bandwidth azimuth resolution and the expression for degraded azimuth resolution for $N_l$ inherent looks is written as

$$\rho'_{aN} = \rho_{aN}\sqrt{1 + \frac{1}{N_l^2}\left[\frac{4\pi}{\lambda}\left(\frac{T_0}{2}\right)^2 a_r(x_g, y_g)^2\right]^2 + \left(\frac{T_0}{\tau_s}\right)^2} \tag{16}$$

where, $T_0$ is the full-bandwidth SAR coherent integration time, and $\tau_s$ is a scene coherence time closely related with the spread of the facet velocities. The detail discussion can be found in [30]. $a_r(x_g, y_g)$ is the derivative of radial velocity $u_r$ with respective to time. $\lambda$ is the radar wavelength. $f_{\rm SAR}(x_g, y_g)$ is the modulation function of SAR imaging

$$f_{\rm SAR}(x_g, y_g) = 2{\rm Re}\int M(\mathbf{k})F(\mathbf{k})e^{i\mathbf{k}\cdot\mathbf{r}}d\mathbf{k} \tag{17}$$

where $F(\mathbf{k})$ is the 2-D Fourier transform of the surface elevations and $M(\mathbf{k})$ is the modulation transfer function

$$M(\mathbf{k}) = M_t(\mathbf{k}) + M_h(\mathbf{k}) \tag{18}$$

$$\begin{aligned} M_t(\mathbf{k}) &= i\frac{k_{||}\partial\sigma_I/\partial s_p + k_\perp \partial\sigma_I/\partial s_n}{\sigma_I}\Big|_{s_{n,p}=0} \\ M_h(\mathbf{k}) &= -4.5\,|\mathbf{k}|\,\omega(\mathbf{k})\,\frac{\omega(\mathbf{k}) - i\mu}{\omega^2(\mathbf{k}) + \mu^2}\sin^2\phi_i \end{aligned} \tag{19}$$

$s_n = \partial_x h(\mathbf{r})$ and $s_p = \partial_y h(\mathbf{r})$ are the local wave slopes, which define the local incidence angle of electromagnetic wave on a facet. $k_{||}$ and $k_\perp$ are the components of the wave vector parallel and normal to the radar line of sight. $\mu$ is the relaxation time constant which reflects the speed of generation and attenuation for small scale wave.

Similar to the form of wave height, the orbital velocity field of the wind driven surface can be described as a linear superposition of the orbital velocities of monochromatic waves by

$$\begin{aligned} u_s(\mathbf{r}) \;=\; \sum_{\mathbf{k}} \Big[ & -j\omega(\mathbf{k})b(\mathbf{k})G(\mathbf{k})\Upsilon(\mathbf{k})\sqrt{\Phi(\mathbf{k},\varphi)\delta k_x \delta k_y/2}\exp\left(-j\omega(\mathbf{k})t\right) \\ & + j\omega(-\mathbf{k})b(-\mathbf{k})G^*(-\mathbf{k})\Upsilon^*(-\mathbf{k})\sqrt{\Phi(\mathbf{k},\pi-\varphi)\delta k_x \delta k_y/2}\exp\left(j\omega(-\mathbf{k})t\right)\Big]\exp(j\mathbf{k}\cdot\mathbf{r}) \end{aligned} \tag{20}$$

where

$$b(\mathbf{k}) \;=\; \sin c(\frac{k_x\Delta x}{2})\cdot\sin c\left(\frac{k_y\Delta y}{2}\right)\cdot\sin c\left[\frac{\omega(\mathbf{k})\,T_0}{2}\right] \tag{21}$$

$$G(\mathbf{k}) \;=\; \cos\theta_i - j\sin\theta_r\sin\theta_i \tag{22}$$

$\theta_r$ means the angle between wave number $\mathbf{k}$ and the moving direction of the radar platform.

However, the derivation of the fluid velocity potential is discussed in detail in [32] which is based on the Michell thin ship theory. Here we provide the expression for the fluid velocity potential as follows

$$\Psi_w(x,y,z) = -\frac{16BL}{\pi}U_s Fr^6 \mathrm{Re}\int_0^\infty C(\nu,x,z)e^{jy\tau}d\nu \tag{23}$$

where $Fr = U_s/\sqrt{gL}$ is the Froude number, the expression of $C(\nu,x,z)$ can be found in [32]. The fluid velocity of ship wake waves can therefore be obtained by calculating the gradient of fluid velocity potential $\Psi_w$

$$u_w(\mathbf{r}) = \nabla\Psi_w(x,y,z) = (u_x,u_y,u_z) \tag{24}$$

A linear superposition of the wind driven surface waves and the ship wake waves gives the total orbital velocity field of the ocean surface

$$u_r(x_g,y_g) = \bar{u}_s(x_g,y_g) + \bar{u}_w(x_g,y_g) \tag{25}$$

The symbol "$-$" means the projection of orbital velocity in the radial direction of SAR.

## 5. NUMERICAL RESULTS AND ANALYSIS

In this section, the attention is devoted to the simulations of SAR image under a variety of conditions. As illustrated in Figure 7, the procedure of SAR imaging of sea surface waves with Kelvin wake can be divided into three main steps: geometric modeling, electromagnetic modeling, and radar imaging model. The characteristics of the radar used in the simulations are listed in Table 1. The X-band and $HH$-polarization are only considered for that the X-band has been widely used in marine radar. According to Hennings et al. [10], $HH$-polarization might be better for wake detection. It is assumed that radar platform travels along the positive $y$-direction.

**Table 1.** Simulation parameters for radar imaging.

| Variable | Value | Variable | Value |
|---|---|---|---|
| $\lambda$ | 0.03 m | $\theta_i$ | 40° |
| $\rho_a$ | 6.0 m | $T_0$ | 0.2 s |
| $R/V$ | 80 s | $N_l$ | 2 |

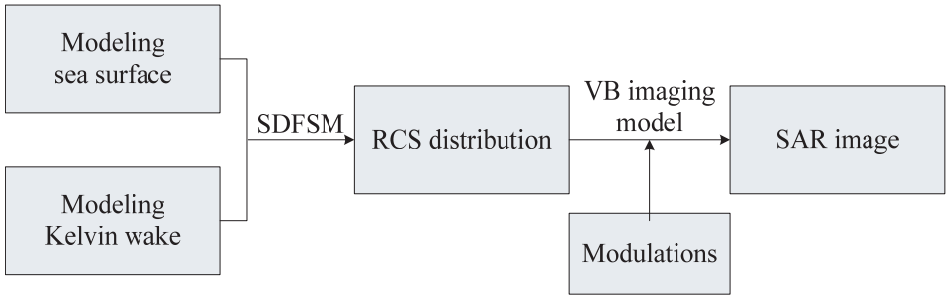


**Figure 7.** Procedure of SAR imaging of sea surface waves with Kelvin wake.

### 5.1. Simulation of SAR Images for Different Ship Speeds

Ship speed as an important parameter is first discussed at a relative low sea state in the simulations and the results are shown in Figure 8. The simulation suggests that the wake pattern become clearer

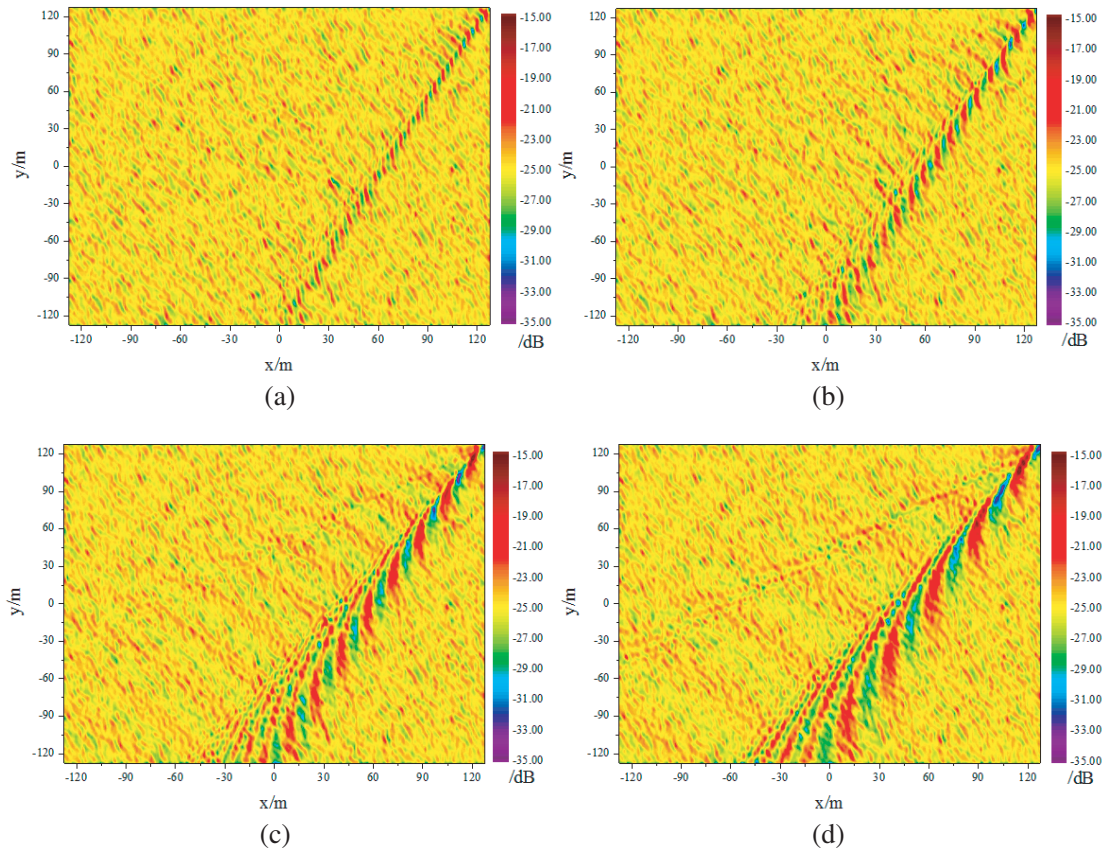


**Figure 8.** SAR images of surface wave with different ship speed, wind speed $U = 3.0\,\mathrm{m/s}$. (a) Ship speed $U_s = 3.0\,\mathrm{m/s}$. (b) Ship speed $U_s = 5.0\,\mathrm{m/s}$. (c) Ship speed $U_s = 7.0\,\mathrm{m/s}$. (d) Ship speed $U_s = 9.0\,\mathrm{m/s}$.

with increasing sailing speed from 3.0 m/s to 9.0 m/s with an interval of 2.0. For this specific traveling direction, there is almost one side of the divergent wave that can be seen from the images and this will be explained later. Besides, the wavelengths for both transverse and divergent waves shown in the SAR images are also increases at a larger ship speed.

### 5.2. Simulation of SAR Images for Different Wind Speeds

Considering that the visibility of ship wake has a strong dependence on the sea clutter, Figure 9 shows the effect of increasing wind speed for different sea states on the simulated SAR images. The ship moves with a constant speed $U_s = 9.0$ m/s. It can be seen that both the transverse and divergent waves are clear in the low sea state, such as $U = 3.0$ m/s in Figure 9(a), and deteriorate as the wind speed increases to $U = 7.0$ m/s. As we further increase the wind speed to $U = 9.0$ m/s, the features of the wake can hardly be resolved from the sea clutter.

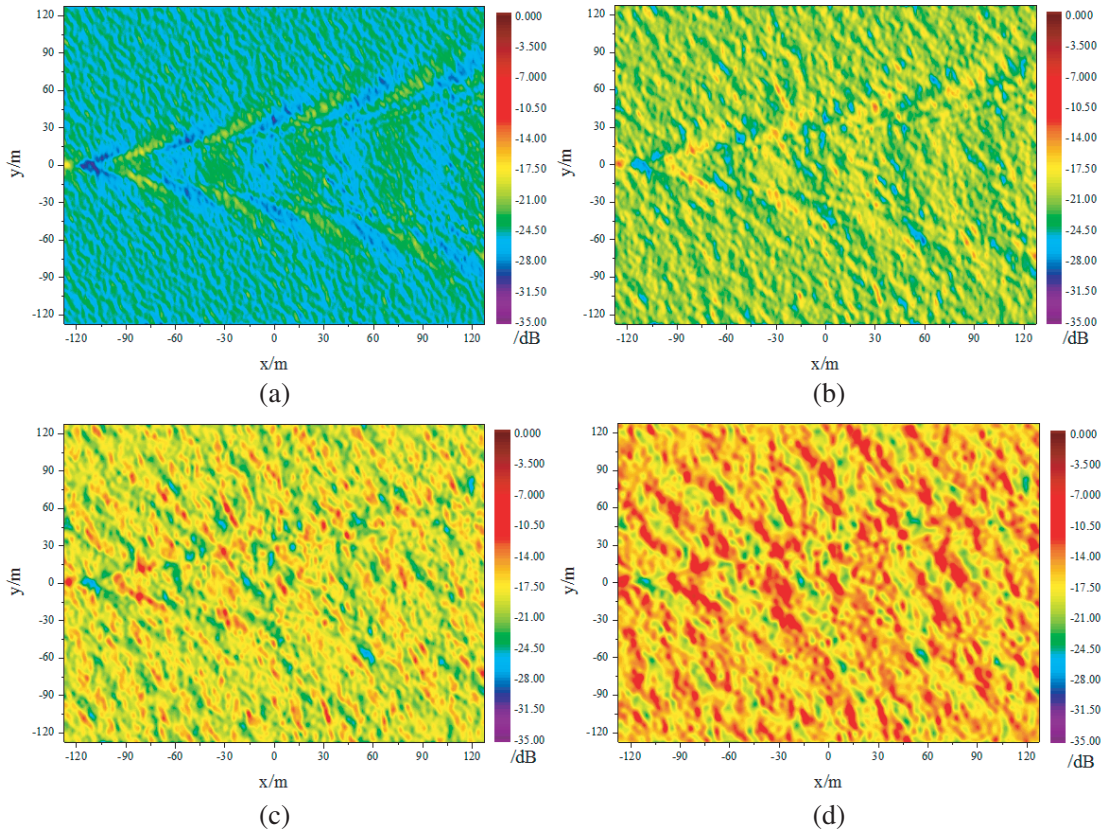


**Figure 9.** SAR images of surface wave with different wind speed, ship speed $U_s = 9.0$ m/s. (a) Wind speed $U = 3.0$ m/s. (b) Wind speed $U = 5.0$ m/s. (c) Wind speed $U = 7.0$ m/s. (d) Wind speed $U = 9.0$ m/s.

### 5.3. Simulation of SAR Images for Different Ship Headings

According to the assumption of Bragg scattering theory, the compositions of surface wave moving parallel to the radar line of sight (LOS) with a satisfaction for the condition of Bragg resonant contribute to the radar scattering echoes. While the cusp waves travel towards the radar, the contributions of tilt and hydrodynamic modulation to the mean NRCS are both positive. On the other hand, it would be imaged as dark stripes as the associated cusp waves propagate normal to the radar look direction. Therefore, it is necessary to discuss the influence on radar image under different traveling directions of a ship, as is illustrated in Figure 10. The sea surface is generated at wind speed of 3.0 m/s and $\varphi_s$ is

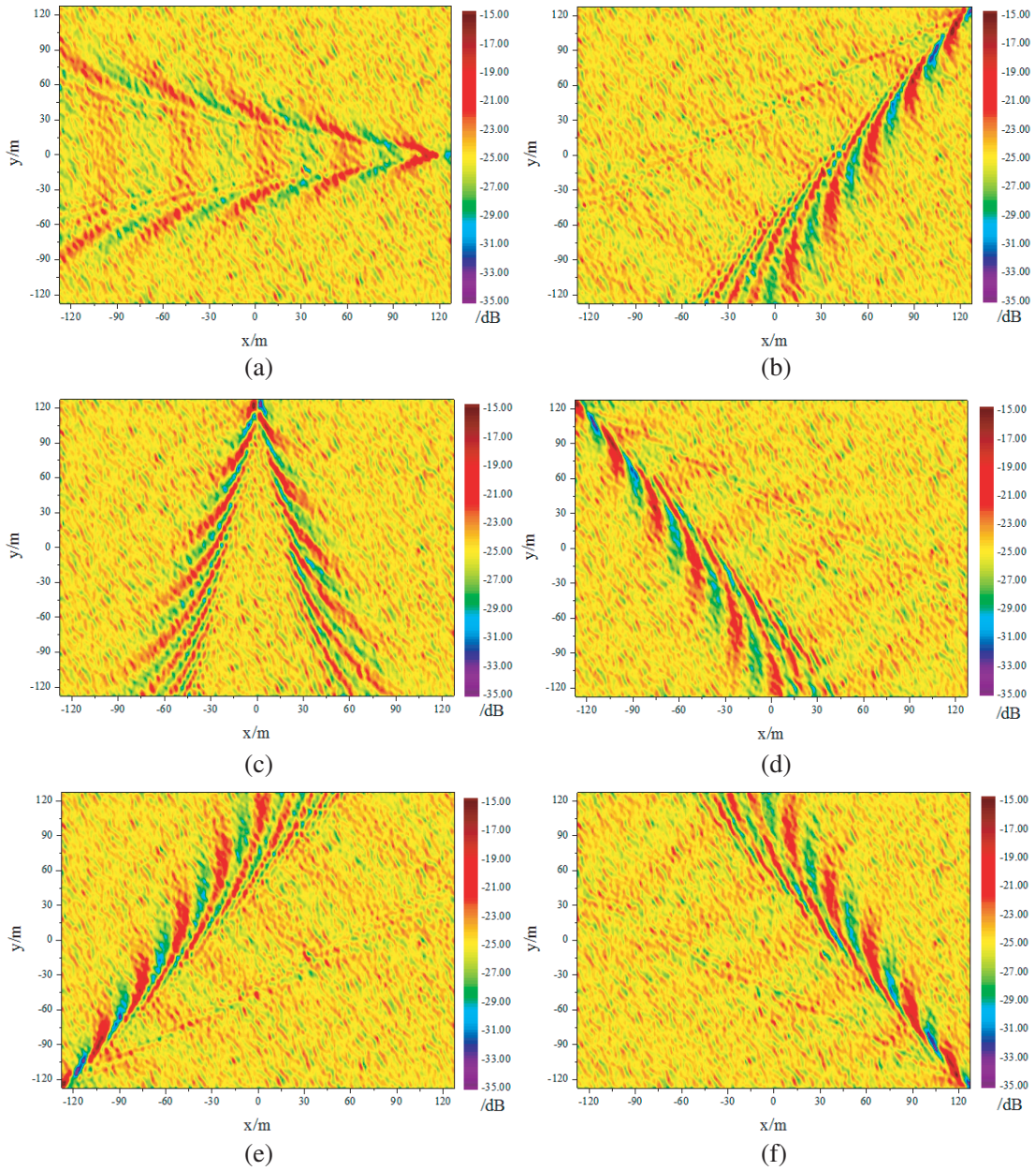


**Figure 10.** SAR images of surface wave with different ship sailing directions, $\varphi_s$ is the angle between the ship track and the positive $x$-axis. (a) Ship heading $\varphi_s = 0°$. (b) Ship heading $\varphi_s = 45°$. (c) Ship heading $\varphi_s = 90°$. (d) Ship heading $\varphi_s = 135°$. (e) Ship heading $\varphi_s = 210°$. (f) Ship heading $\varphi_s = 315°$.

defined as the angle between the ship track and the positive $x$-direction. From the results, it can be seen the wake features are well visible but with different manifestations for different angles. The whole wake is clearly shown for the ship with a movement parallel to the LOS in Figure 10(a), whereas the transverse waves become invisible while $\varphi_s = 90°$ for that they movement is vertical to the LOS and makes little contributions to the scattering of surface waves. However, as for the general cases, one arm of the Kelvin wake is clear to see and the other features weak, as shown in Figures 10(b), (d), (e) and (f). The bright arm is always close to the LOS. Comparison between (b) and (d) shows that the closer to $x$-axis, the obscurer for the weak arm, which can also be found from (e) and (f).

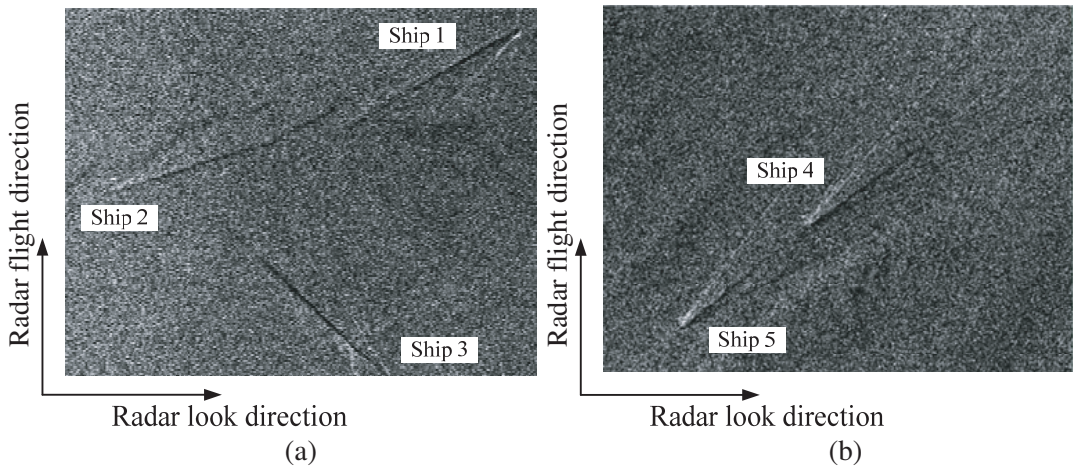


**Figure 11.** Enlarged image section of the SEASAT SAR scene: (a) East coast of Jütlandin the Baltic Sea from ORBIT 1249. (b) Southern bight of the North Sea from orbit 1473.

Figure 11 shows two SEASAT L-bands $HH$ polarized SAR images under different ship travel directions under low to moderate wind speeds [15]. Regardless of the turbulent wake appearing as a narrow dark streak along the ship track, it is evident in Figure 11(a) that the right-hand Kelvin arm of ship 1 ($\varphi_s = 40°$), the left-hand Kelvin arm of ship 2 ($\varphi_s = 220°$) and the left-hand Kelvin arm of ship 3 ($\varphi_s = 310°$) are visible as bright streaks, which perform similar features as Figures 10(b), (e) and (f). The wake characteristic is shown more obvious by ship 4 and ship 5 in Figure 11(b), both of which are moving with an angle of $\varphi_s = 228°$ relative to the radar look direction. However, the experiments SAR images are done with respect to a relative wide ocean scene. It can hardly be seen for the detail features of transverse and divergent waves.

## 6. CONCLUSIONS

According to the hydrodynamic model of Kelvin wake and sea surface wave, the application of velocity bunching (VB) imaging model for SAR imagery of ship wakes with different parameters is studied based on the semi-deterministic facet scattering model (SDFSM), which can be applied to the simulation of the radar backscattering echo. From the numerical results of backscattering NRCS, there is a good agreement with the experiment by SASS-II for both $VV$ and $HH$ polarizations in most instances except for the region near vertical incidence. As for the simulated SAR images, ship speed affects the wave height of Kelvin wake greatly. Besides, the visibility of Kelvin wake is strongly dependent on the wind speed and is always clear to see in low sea states but deteriorates with the increasing wind speed. Furthermore, the manifestation of wake pattern usually varies with the ship sailing direction.

However, there are turbulent wake and internal wave wake as well excited by a moving ship. Further study can be focused on the theoretical modeling and SAR imaging of these two wakes so as to detect a ship from its wake features.

## ACKNOWLEDGMENT

This work was supported in part by the Fundamental Research Funds for the Central Universities, the National Nature Science Foundation of China under Grant No. 61372004/41306188, and the Foundation of Science and Technology on Electromagnetic Scattering Laboratory.

## REFERENCES

1. Holt, B., "SAR imaging of the ocean surface," *Synthetic Aperture Radar Marine User's Manual*, 25–79, C. R. Jackson and J. R. Apel (eds.), NOAA, Washington, 2004.

2. Zhang, Y. D., L. N. Wu, and G. Wei, "A new classifier for polarimetric SAR images," *Progress In Electromagnetics Research*, Vol. 94, 83–104, 2009.
3. Liu, X. W., "Remote sensing image classification of the improved BP NN," *Journal of Sustainable Development*, Vol. 3, No. 4, 220–225, 2010.
4. Lyden, J. D., R. R. Hammond, D. R. Lyzenga, and R. A. Shuchman, "Synthetic aperture radar imaging of surface ship wakes," *J. Geophys. Res.*, Vol. 93, 12293–12303, 1988.
5. Reed, A. M. and J. H. Milgram, "Ship wakes and their radar images," *Annual Review of Fluid Mechanics*, Vol. 34, 469–502, 2002.
6. William, G. P., C. C. Pablo, C. W. Christopher, and S. F. Karen, "Ship and wake detection," *Synthetic Aperture Radar Marine User's Manual*, 277–303, C. R. Jackson and J. R. Apel, Eds., NOAA, Washington, 2004.
7. Tunaley, J. K. E., E. H. Buller, K. H. Wu, and M. T. Rey, "The simulation of the SAR image of a ship wake," *IEEE Trans. Geosci. Remote Sens.*, Vol. 29, 149–156, 1991.
8. Oumansour, K., Y. Wang, and J. Saillard, "Multi-frequency SAR observation of a ship wake," *IEE Proc. Radar, Sonar Navig.*, Vol. 143, No. 4, 275–280, 1996.
9. Shemer, L., L. Kagan, and G. Zilman, "Simulation of ship wake image by an along-track interferometric SAR," *Int. J. Remote Sens.*, Vol. 17, 3577–3597, 1996.
10. Hennings, I., R. Romeiser, W. Alpers, and A.Viola, "Radar imaging of Kelvin arms of ship wakes," *Int. J. Remote Sens.*, Vol. 20, 2519–2543, 1999.
11. Zilman, G., A. Zapolski, and M. Marom, "The speed and beam of a ship from its wake's SAR images," *IEEE Trans. Geosci. Remote Sens.*, Vol. 42, 2335–2343, 2004.
12. Wang, A.-M. and M.-H. Zhu, "Simulation of ship generated turbulent and vertical wake imaging by SAR," *Journal of Electronics*, Vol. 21, 64–71, 2004.
13. Arnold-Bos, A., A. Khenchaf, and A. Martin, "Bistatic radar imaging of the marine environment — Part II: Simulation and result analysis," *IEEE Trans. Geosci. Remote Sens.*, Vol. 45, 3384–3396, 2007.
14. Sun, R.-Q., G. Luo, M. Zhang, and C. Wang, "Electromagnetic scattering model of the Kelvin wake and turbulent wake by a moving ship," *Waves in Random Media*, Vol. 21, 501–514, 2011.
15. Zilman, G., A. Zapolski, and M. Marom, "On detectability of a ship's Kelvin wake in simulated SAR images of rough sea surface," *IEEE Trans. Geosci. Remote Sens.*, Vol. 53, 609–619, 2014.
16. Voronovich, A. G., *Wave Scattering from Rough Surfaces*, 2nd Edition, Springer-Verlag Berlin, Heidelberg, New York, 1999.
17. Pinel, N. and C. Boulier, *Electromagnetic Wave Scattering from Random Rough Surfaces: Asymptotic Models*, Wiley-ISTE, 2013.
18. Soubret, A., G. Berginc, and C. Bourrely, "Application of reduced Rayleigh equations to electromagnetic wave scattering by two-dimensional randomly rough surfaces," *Physical Review B*, Vol. 63, No. 24, 245411, 2001.
19. Elfouhaily, T. and C.-A. Guerin, "A critical survey of approximate scattering wave theories from random rough surfaces," *Waves in Random Media*, Vol. 14, No. 4, R1–R40, 2004.
20. Ulaby, F., R. Moore, and A. Fung, *Microwave Remote Sensing: Active and Passive, Vol. 2 — Radar Remote Sensing and Surface Scattering and Emission Theory*, Addison-Wesley, Advanced Book Program, Reading, MA, 1982.
21. Voronovich, A., "Small-slope approximation for electromagnetic wave scattering at a rough interface of two dielectric half-spaces," *Waves in Random Media*, Vol. 4, No. 3, 337–367, 1994.
22. Voronovich, A. and V. Zavorotny, "Theoretical model for scattering of radar signals in Ku- and C-bands from a rough sea surface with breaking waves," *Waves in Random Media*, Vol. 11, No. 3, 247–269, 2001.
23. Tessendorf, J., "Simulating ocean water," *Simulating Nature: Realistic and Interactive Techniques, ACM SIGGRAPH 2001 Course Notes*, 2001.
24. Elfouhaily, T., B. Chapron, and K. Katsaros, "A unified directional spectrum for long and short wind-driven waves," *J. Geophys. Res.*, Vol. 102, 15781–15796, 1997.

25. Fuks, I. M. and A. G. Voronovich, "Wave diffraction by rough interfaces in an arbitrary plane-layered medium," *Wave in Random Media*, Vol. 10, 253–272, 2000.
26. Fuks, I. M., "Wave dirrfaction by a rough boundary of an arbitrary plane-layered medium," *IEEE Trans. Antennas Propagat.*, Vol. 49, 630–639, 2001.
27. Chen, H., M. Zhang, D. Nie, and C. C. Yin, "Robust semi-deterministic facet model for fast estimation on EM scattering from ocean-like surface," *Progress In Electromagnetics Research B*, Vol. 18, 347–363, 2009.
28. Arnold-Bos, A., A. Khenchaf, and A. Martin, "Bistatic radar imaging of the marine environment — Part I: Theoretical background," *IEEE Trans. Geosci. Remote Sens.*, Vol. 45, 3372–3383, 2007.
29. Zhang, M., Y.-W. Zhao, H. Chen, and W.-Q. Jiang, "SAR imaging simulation for composite model of ship on dynamic ocean scene," *Progress In Electromagnetics Research*, Vol. 113, 395–412, 2011.
30. Zurk, L. and W. Plant, "Comparison of actual and simulated synthetic aperture radar image spectra of ocean waves," *J. Geophys. Res.*, Vol. 101, No. C4, 8913–8931, 1996.
31. Zhao, Y. W., M. Zhang, X. Geng, and P. Zhou, "A comprehensive facet model for bistatic SAR imagery of dynamic ocean scene," *Progress In Electromagnetics Research*, Vol. 123, 427–445, 2012.
32. Newman, J. N., *Marine Hydrodynamics*, M.I.T. Press, Cambridge, Mass, 1977.